Experimental Study of Real-Time Human Imaging Using UWB Doppler Radar Interferometry

Kenshi Saho, Takuya Sakamoto, and Toru Sato
Graduate School of Informatics
Kyoto University
Kyoto, Japan 606–8501
E-mail: k.saho@e06.mbox.media.kyoto-u.ac.jp

Kenichi Inoue and Takeshi Fukuda
Advanced Technology Research Laboratories
Panasonic Corporation
Kyoto, Japan 619–0237

***Abstract*—This study presents an algorithm for imaging humans with Ultra Wide-Band (UWB) Doppler radar and experimental examples of its application. The proposed algorithm estimates the scattering centers using interferometry. Furthermore, we propose a false image rejection method with velocity information. Our experiments, which assume a pedestrian, show that the proposed algorithm is capable of imaging humans in a realistic environment. In addition, we discuss the real-time performance of the proposed imaging algorithm. The time variations for the estimated image indicate that pedestrian identification can be realized even using real-time data.**

I. Introduction

Imaging and identification of humans with radar has great potential for use in surveillance systems. For this purpose, numerous studies have been conducted using micro-Doppler radar [1]– [5]. These studies investigated the extraction of human features based on time-frequency micro-Doppler signatures. For example, the classification of motion types (running, walking, walking without arm-motion, and so on) was achieved in [4], [5]. However, the primary aim of these studies was feature extraction or positioning to the order of 10 cm, which made it difficult to estimate details of humans, such as shape information.

For human imaging and tracking, Lin and Ling [6]– [8] proposed continuous wave (CW) Doppler radar interferometric imaging, which separates multiple targets using the differences in their Doppler frequencies and extracts the direction-of-arrival (DOA) of each target with interferometry. However, this method generates many false images due to interference from multiple targets and inadequate resolution. To resolve these problems, we proposed an Ultra Wide-Band (UWB) Doppler radar interferometric imaging method, and achieved high-resolution shape estimation of simple-shaped multiple moving targets [9]. However, this method also generates false images because of interference.

In this study, we apply the UWB Doppler radar interferometric imaging method [9] to human imaging. To reduce the occurrence of false images in the interferometry, we clarify the way in which they are created and propose a false image detection and rejection method using velocity information. We experimentally verify that the proposed rejection method reduces false images and realizes satisfactory human imaging. In addition, we consider the time variation of estimated human images for a real-time surveillance system. The experimental results show that real-time human identification can be realized by our proposed imaging algorithm.

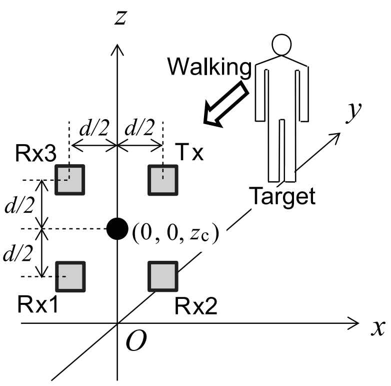

Fig. 1. System model.

II. Basic UWB Doppler radar interferometric imaging method

Figure 1 shows the system model. We set a transmitting antenna Tx and three receiving antennas, Rx1, 2, and 3, in an xz plane. An interferometer is composed of these receiving antennas. The central point of the antennas is (0, 0, $z_{\rm c}$), and the positions of Tx, Rx1, Rx2, and Rx3 are expressed as (x, z) = (d/2, $d/2$+$z_{\rm c}$), (-d/2, -$d/2$+$z_{\rm c}$), (d/2, -$d/2$+$z_{\rm c}$) and (-d/2, $d/2$+$z_{\rm c}$). The transmitting signal is a UWB spread spectrum signal with a central frequency of f_0. The bandwidth is W, which corresponds to a downrange resolution of $\Delta R = {\rm c}/2W$, where c is the speed of light. We acquire the received signal $s_{ij}(t)$ in the range bin j using Rxi.

The basic UWB Doppler radar interferometric imaging method separates multiple targets using time-frequency distribution [6], [7]. If different moving targets have different radial velocities, we can separate them by the differences in their Doppler frequencies. Since human body parts such as arms and legs generally have different motions, we regard them as multiple moving targets. In this study, time-frequency distribution $S_{ij}(t, v_{\rm d})$ is obtained using the sliding-window Discrete Fourier Transform (SDFT) [10] of $s_{ij}(t)$, where $v_{\rm d}$

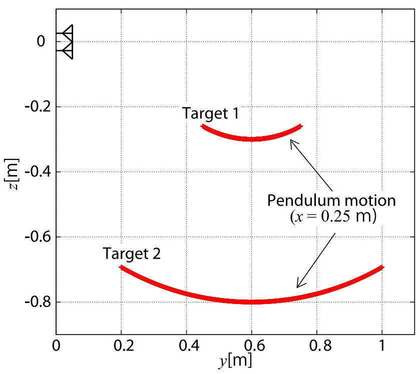

Fig. 2. Orbit of targets in the numerical simulation.

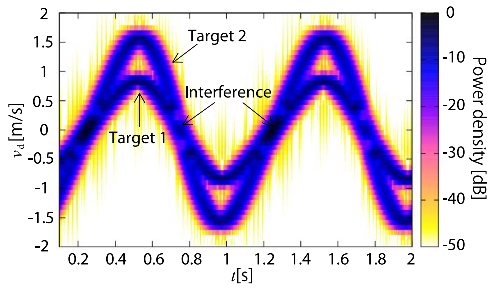

Fig. 3. Acquired spectrogram in the simulation.

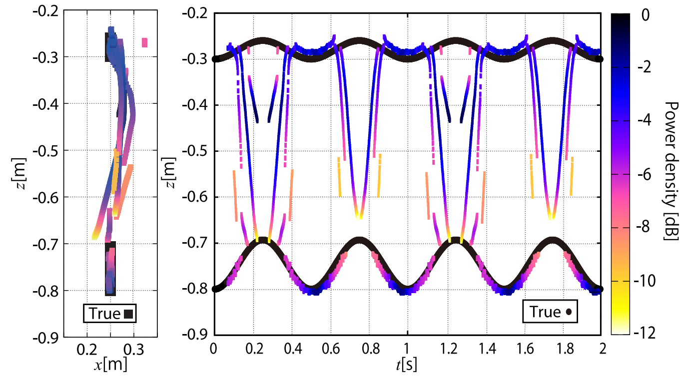

(a) (b)

Fig. 4. Estimated image in the simulation: (a) frontal view. (b) $z(t)$.

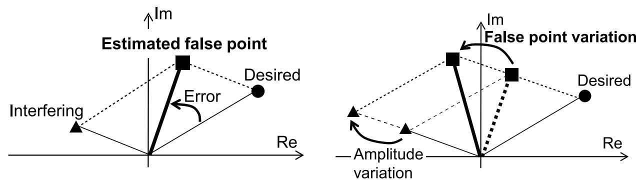

(a) (b)

Fig. 5. Outline of the mechanism for creating false images: (a) effect on interference. (b) effect on amplitude variation.

is the radial velocity. Sufficient peaks corresponding to each target are extracted from $S_{ij}(t, v_{\mathrm{d}})$.

The positions of the scattering centers that correspond to each separated target are then estimated by mapping the $t - v_{\mathrm{d}}$ of each on a plane of distance and direction of arrival (DOA). The elevation DOA $\theta_{\mathrm{EL}n}$ and azimuth DOA $\theta_{\mathrm{AZ}n}$ of the nth target are estimated using the interferometry by

$$\theta_{\mathrm{EL}n}(t) = \sin^{-1}\left[\frac{\angle S_{1j'}(t, v_{\mathrm{d}n}) - \angle S_{3j'}(t, v_{\mathrm{d}n})}{(2\pi d/\lambda)}\right], \quad (1)$$

$$\theta_{\mathrm{AZ}n}(t) = \sin^{-1}\left[\frac{\angle S_{1j'}(t, v_{\mathrm{d}n}) - \angle S_{2j'}(t, v_{\mathrm{d}n})}{(2\pi d\cos\theta_{\mathrm{EL}n}/\lambda)}\right], \quad (2)$$

where λ is the wavelength and j' is the range bin in which a target is detected. The distance R_n is estimated by finding the range that maximizes the echo intensity with interpolation between the range gates [9]. With the acquired R_n, $\theta_{\mathrm{AZ}n}$ and $\theta_{\mathrm{EL}n}$, we estimate the position of each scattering center.

III. False Image Detection and Rejection Method

A. Example of a False Image and the Mechanism of Its Creation

The basic UWB Doppler radar interferometric imaging method, however, generates many false images because it assumes all scattering centers have different radial velocities. In this subsection, we show an example of such false images and clarify the mechanism of their creation with a simple numerical simulation which focuses on their detection. Fig. 2 shows the orbits of the targets in the simulation. We assume two point targets having a pendulum motion and set the antenna separation at d=5 mm and the center position of the antennas at z_{c}=0. The parameters of the transmitting signals are f_0=26.4 GHz and W=500 MHz, which corresponds to ΔR=30 cm. Omni-directional antennas are assumed, and the received signals are determined by ray-tracing.

Figures 3 and 4 show the spectrogram and the estimated image. False images are estimated where the target does not exist. Comparing Figs. 3 and 4 (b), we find that false images are generated when interference of the echoes occurs. The DOA is estimated by means of the phase difference between the two antennas, as expressed in Eqs. (1) and (2); however, phase estimation errors are caused by the interference. Fig. 5(a) outlines the phase estimation error at an antenna, where the horizontal and vertical axes are the real and imaginary parts of a received echo. Since this error is caused at all antennas, the estimated phase differences also have errors. The amplitude variation of the echo leads to fast motion of the false images. Fig. 5(b) outlines the effect on the amplitude variation, which also causes phase error. For example, in Fig. 3, the amplitude ratios of targets 1 and 2 vary from 1.26 to 1.45 over 0.2 s $< t <$ 0.3 s, and the scattering centers corresponding to these data move at approximately 4 m/s. This velocity is larger than the maximum speed of the assumed target, which is 2.5 m/s. Thus, many false images have a velocity greater than the maximum speed assumed by the type of motion.

B. Proposed False Image Rejection Method

Based on the discussion in the previous subsection, we propose a false image detection and rejection method. We

Fig. 6. Experimental site for a pedestrian target on a treadmill.

reject the estimated scattering centers with relatively large velocities that satisfy the following condition:

$$v_{\max} < |\mathbf{v}(t, v_{\mathrm{d}})|, \tag{3}$$

where $\mathbf{v}(t, v_{\mathrm{d}})$ is the velocity estimated as the time-derivative of the movement of a scattering center position and $v_{\max}$ is the assumed maximum speed. In addition, isolated points are removed. We assume a sphere with radius R_{F} whose center is at $\mathbf{x}_{\mathrm{s}}(t, v_{\mathrm{d}n})$ and count the number of estimated scattering centers N_{F} within it. We reject the scattering centers that satisfy the condition

$$N_{\mathrm{F}}/N_{\mathrm{A}} < \alpha, \tag{4}$$

where N_{A} is the total number of estimated points and $\alpha < 1$ is empirically determined by the spatial resolution.

IV. Experimental Results and Discussion

A. Experimental Setup

This section shows the effectiveness of our proposed false image rejection method in our human imaging experiments. In addition, for real-time imaging, we investigate the time variation of the estimated images. The radar parameters are d=3.5 cm, f_0=26.4 GHz, W=500 MHz, and ΔR=30 cm. We use horn antennas with -3 dB beamwidth of $\pm 11^\circ$ in both the E-plane and H-planes. The inter pulse period is 1.29 ms, and the window size for the SDFT is 165 ms. We take measurements in some antenna positions, and an image is generated by the superposition of the scattering centers estimated for each antenna position.

B. Application to a Pedestrian Target on a Treadmill

This subsection assumes a human subject walking on a treadmill at a belt speed of 3 km/h. Fig. 6 shows the experimental site. The distance between the center of the antennas and the examinee is 2.7 m. The heights of the examinee and the treadmill are 182 and 14 cm. We measured at three antenna positions: z_{c}=0.56, 1.26, and 1.81 m. Fig. 7 shows the spectrogram of the range bin 9 (2.7 m) for z_{c} =1.26 and 0.56 m. The radial velocity variation of the arms and legs and the

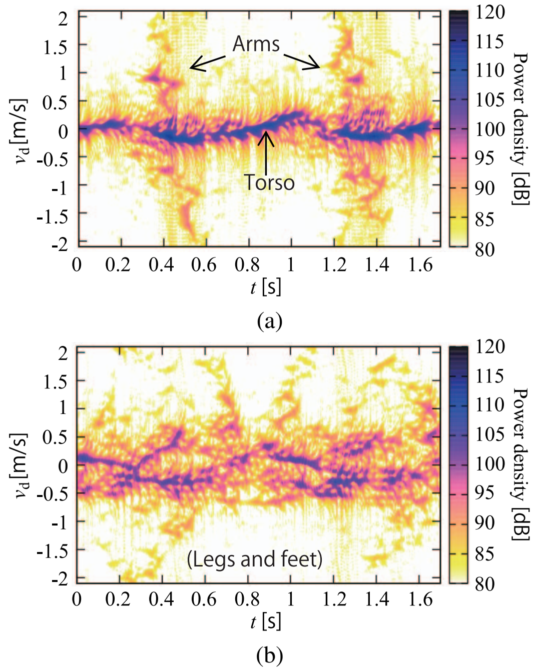

Fig. 7. Spectrogram $|S_{19}(t, v_{\mathrm{d}})|^2$ for (a) $z_{\mathrm{c}} = 1.26$ m and (b) 0.56 m.

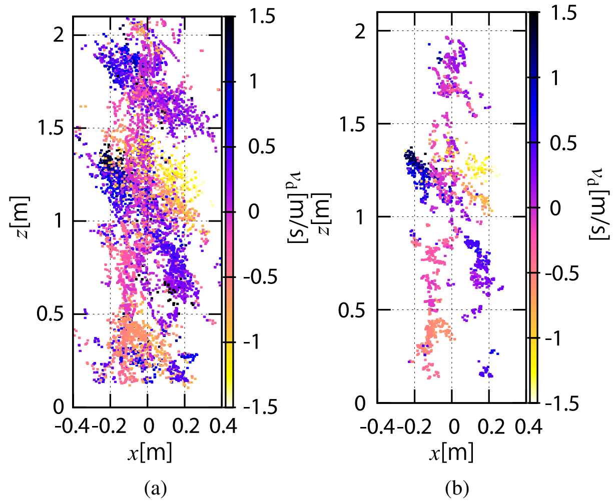

Fig. 8. Frontal view of estimated image: (a) using only the UWB Doppler radar interferometric imaging method; (b) using the proposed false image rejection method.

body oscillations are detected. Fig. 8(a) shows the frontal view of the image estimated using only the basic UWB Doppler radar interferometric imaging method. Here, we used the data from half a walking cycle (t <0.78 s). We are not able to identify the human because of many false images. Fig. 8(b) shows the estimated image after applying the proposed false image rejection method to the data of Fig. 8(a). We empirically set $v_{\max}$ =2.5 m/s, R_{F} =3 cm, and $\alpha = 0.003$. Our proposed method rejects almost all the false images and estimates the scattering centers for each of the body parts. This result verifies that our proposed imaging algorithm achieved adequate human

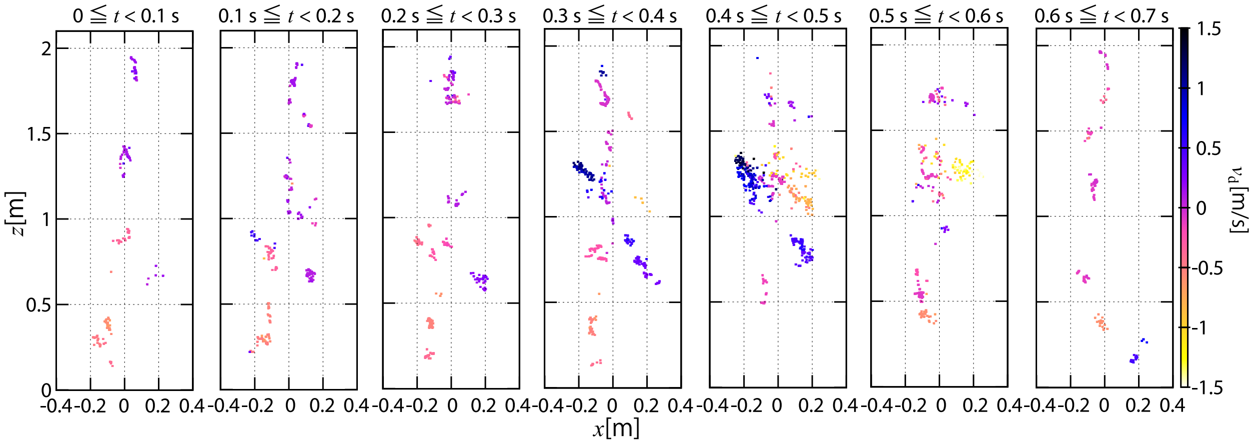

Fig. 9. Time variation of the estimated frontal image of a pedestrian target on a treadmill in $t < 0.7s$.

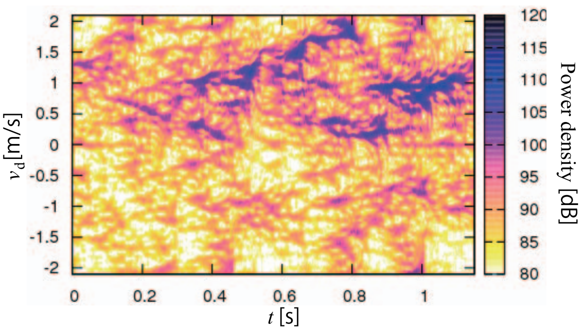

Fig. 10. Summation of spectrograms from $|S_{15}(t, v_\mathrm{d})|^2$ to $|S_{19}(t, v_\mathrm{d})|^2$ for $z_\mathrm{c} = 0.36$ m.

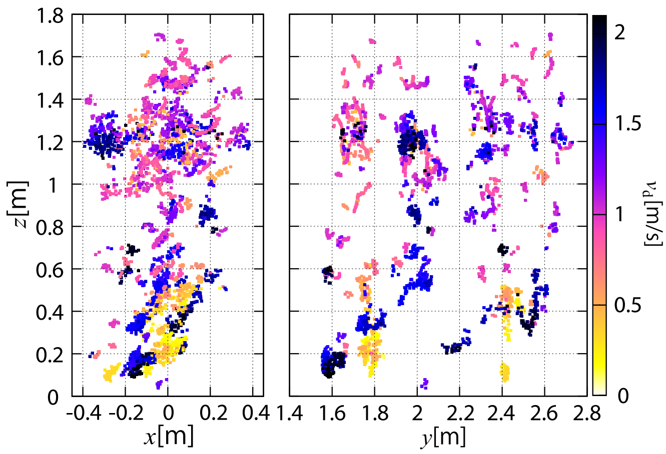

Fig. 11. Frontal (left) and side (right) image of an actual pedestrian estimated by the proposed algorithm.

imaging.

We next investigate the time variation of the estimated image. Fig. 9 shows the time variation of Fig. 8(b) with time steps of 0.1 s at $t < 0.7$ s. We are able to recognize the motion of each body part by comparing Fig. 9 and 8(b). For instance, when the right foot swing forward, we observe the radial velocity and position variations corresponding to this motion. In addition, the left foot have negative radial velocity. As discussed above, a pedestrian's features are detected in Fig. 9. We are able to identify a pedestrian in the real-time imaging system from these results.

C. Application to a Pedestrian Target Walking Toward the Antennas

In this subsection, we assume a pedestrian subject without a treadmill. The examinee walk from $(x, y) = (0, 2.7 \text{ m})$ to $(0, 1.5 \text{ m})$ with a walking cycle of 1.2 s and a mean speed of 1.0 m/s. The height of the examinee is 1.63 m. We measure at four antenna positions: z_c=0.36, 0.82, 1.29, and 1.54 m. Fig. 10 shows the summation of the spectrograms from $|S_{15}(t, v_\mathrm{d})|^2$ to $|S_{19}(t, v_\mathrm{d})|^2$ for $z_\mathrm{c} = 0.36$ m. The radial velocity variation of the legs corresponding to two steps is obtained. In addition, the offset of the spectrograms is the mean walking speed.

Figure 11 shows the image estimated by the proposed algorithm using all the data of Fig. 10. Parameters v_max, R_F, and α have the same values as in the previous subsection. We extract the outline of the human and the radial velocity features of the walking motion. With the side view, we can see the walking motion which corresponds to two steps. In $z < 0.8$ m, the scattering centers with relatively large velocities corresponds to the swinging of the leg, and the scattering centers with small v_d corresponds to the other leg in contact with the ground. Moreover, the arm swinging motion is detected as relatively large velocities over about 0.8 m $< z < 1.3$ m. We can recognize the pedestrian target from these results.

Figures 12 and 13 show the time variation of the frontal and side images with time steps of 0.1 s at $t < 0.6$ s. The pedestrian features are even detected using real-time images. Although the frontal image is distorted because of interference, we can confirm that the time variation of the legs corresponding to the walking motion is the same as in

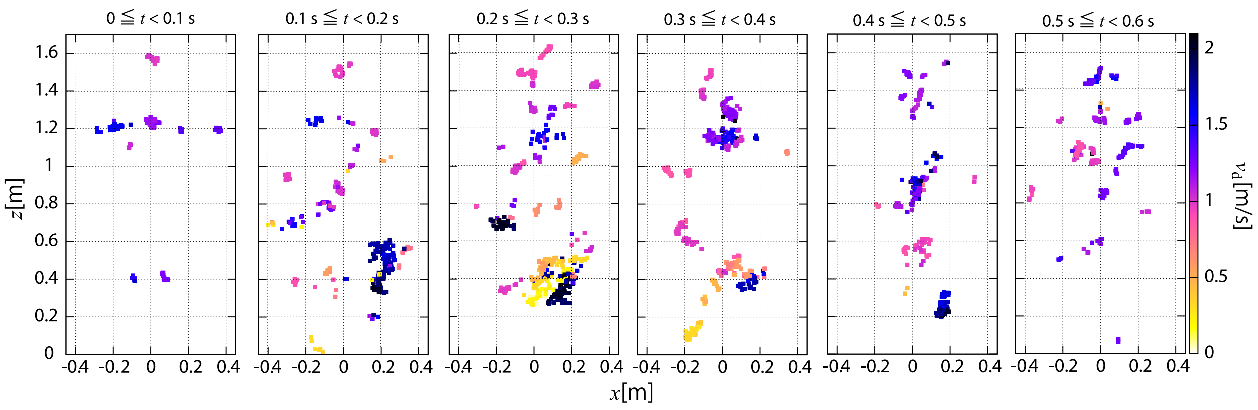

Fig. 12. Time variation of the estimated frontal image of an actual pedestrian target at $t < 0.6s$.

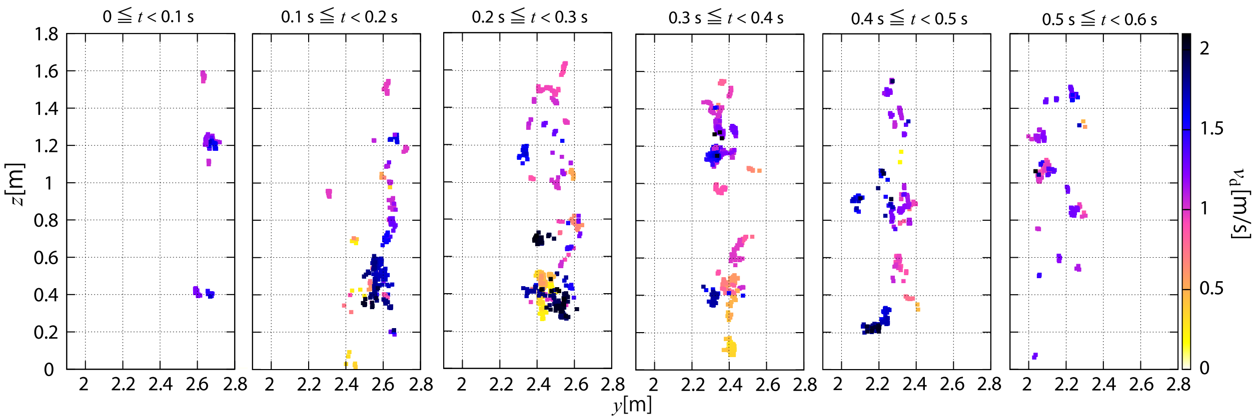

Fig. 13. Time variation of the estimated side image of an actual pedestrian target at $t < 0.6s$.

Fig. 9. Moreover, as shown in Fig. 13, the translation of the body and the swinging of the hands and feet that accompany the walking are confirmed. The time variation of the estimated points with a relatively high velocity at $z < 0.6$ m corresponds to the forward motion of the foot. These results show that we achieved real-time pedestrian identification using the proposed imaging algorithm in a realistic situation.

V. Conclusions

This study demonstrated human imaging using UWB Doppler radar interferometry. We clarified the mechanism for creating false images generated in the interferometry and proposed a false image detection and rejection method. The experiments, which assumed pedestrians, verified that the proposed algorithm achieved adequate human imaging, and pedestrian features were detected during the time variation of the estimated image. These results indicated that real-time human identification can be realized with our proposed imaging algorithm.

References

[1] P. Setlur, F. Ahmad, and M. Amin, "Maximum likelihood and suboptimal schemes for micro-Doppler estimation using carrier diverse Doppler radars," *IET Sign. Proc.*, vol. 5 , no. 2, pp.194–208, 2011.

[2] L. Ying, Z. Qun, Q. Cheng-wei, L. Xian-Jiao, and L. Kai-Ming, "Micro-Doppler Effect Analysis and Feature Extraction in ISAR Imaging With Stepped-Frequency Chirp Signals," *IEEE Trans. Geoscie. Remote Sens.*, vol.48, no. 4, pp. 2087–2098, 2010.

[3] L. Peng, W. Jun, G. Peng, and C. Duoduo, "Automatic classification of radar targets with micro-motions using entropy segmentation and time-frequency features," *Int. J. Electron. Commun. (AEU)*, vol. 65, no. 10, pp. 806–813, 2011.

[4] Y. Kim and H. Ling, "Through-wall human activities classification using support vector machine," *IEEE Trans. Geoscie. Remote Sens.*, vol. 47, pp. 1328–1337, 2009.

[5] I. Orovic, S. Stankovic, and M. Amin, "A new approach for classification of human gait based on time-frequency feature representations," *Signal Processing*, vol. 91, no. 6, pp. 1448–1456, 2011.

[6] A. Lin and H. Ling, "Doppler and direction-of-arrival (DDOA) radar for multiple-mover sensing," *IEEE Trans. Aero. Elec. Sys.*, vol. 43, no. 4, pp. 1496–1509, 2007.

[7] A. Lin and H. Ling, "Frontal imaging of human using three element Doppler and direction-of-arrival radar," *Electronics Letters*, vol. 42, no. 11, pp. 660–661, 2006.

[8] A. Lin and H. Ling, "Three-dimensional tracking of humans using very low complexity radar," *Electronics Letters*, vol. 42, no. 18, pp. 1062–1063, 2006.

[9] K. Saho, T. Sakamoto, T. Sato, K. Inoue, and T. Fukuda, "High-resolution UWB Doppler radar interferometric algorithm for multiple moving targets with smoothed pseudo Wigner distribution," *Int. Conf. on Space, Aeronautical and Navigational Electronics (ICSANE)*, pp. 261–266, 2010.

[10] E. Jacobsen, and R. Lyons, "The Sliding DFT," *IEEE Trans. Sig. Proc. Mag.*, vol. 20, no. 2, pp. 74–80, 2003.